Solution of the fully-mixed-state problem: Direct deperturbation analysis of the $A\,^1\Sigma^+ - b\,^3\Pi$ complex in a NaCs dimer

J. Zaharova, M. Tamanis, and R. Ferber
Laser Center, University of Latvia, 19 Rainis Boulevard, Riga LV-1586, Latvia

A. N. Drozdova, E. A. Pazyuk, and A. V. Stolyarov
Department of Chemistry, Moscow State University, GSP-2 Leninskie gory 1/3, Moscow 119992, Russia
(Received 28 October 2008; published 20 January 2009)

Laser-induced fluorescence (LIF) spectra (4) $^1\Sigma^+ \rightarrow A\,^1\Sigma^+ - b\,^3\Pi$ and collisionally enhanced $A\,^1\Sigma^+ - b\,^3\Pi \rightarrow X\,^1\Sigma^+$ LIF spectra measured by Fourier transform spectrometer with the resolution of 0.03–0.05 cm^{-1} provided about 1160 term values of the *e*-symmetry rovibronic levels of the fully mixed $A\,^1\Sigma^+$ and $b\,^3\Pi$ states of a NaCs molecule. Direct deperturbation treatment of the experimental data field, covering rotational quantum numbers $J \in [5,151]$ of the *A*-*b* complex in the energy region $E \in [10577,13668]$ cm^{-1}, was accomplished in the framework of the inverted channel-coupling approach by means of the 4×4 Hamiltonian constructed on Hund's coupling case (*a*) basis functions. The nonequidistant spin-orbit splitting of the $b\,^3\Pi_{\Omega=0,1,2}$ substates and the indirect coupling $A\,^1\Sigma^+ - b\,^3\Pi_{\Omega=1}$ matrix element were introduced in the Hamiltonian phenomenologically to account for the regular perturbations by remote states manifold. The expanded Morse oscillator model was used to approximate both potential energy curves of the mutually perturbed states and spin-orbit coupling matrix elements as an analytical function of internuclear distance. Overall 31 fitting parameters have been required to reproduce 98% of experimental term values with a standard deviation of 0.006 cm^{-1}, which is consistent with the uncertainty of the experiment. The term values deperturbation analysis was confirmed by a calculation of relative intensity distributions in the $A-b \rightarrow X$ LIF progressions. The predicted probabilities for both weakly and strongly perturbed levels agree with their experimental counterparts within the accuracy of measurements. The evaluated nonadiabatic *A*-*b* wave functions were applied for a prediction of radiative lifetimes of the *A*-*b* complex as well as transition probabilities of the $a \rightarrow A-b \rightarrow X$ cycle proposed in Stwalley, Eur. Phys. J. D **31**, 221 (2004), for efficient transformation of ultracold molecules to their absolute ground level $v_X=0$; $J_X=0$.

DOI: 10.1103/PhysRevA.79.012508 PACS number(s): 31.50.−x, 33.50.Dq, 33.70.Fd, 37.10.−x

I. INTRODUCTION

Heteronuclear alkali-metal diatomic molecules are a popular object of theoretical and experimental studies, in particular due to recent progress in the production and trapping of ultracold species; see, for a review, several special issues of journals [1–7]. Particular attraction is caused in heteronuclear alkali-metal diatomic molecules mainly because of their permanent electric dipole moment, which makes them susceptible to controlled manipulation by an external electric field [8]. After accomplishing most of the work on the ground electronic states, there is growing need in high-accuracy conventional spectroscopy data on the lowest excited electronic states of heteronuclear alkali-metal dimers. Indeed, such mixed singlet-triplet states as $A\,^1\Sigma^+ - b\,^3\Pi$ and $B\,^1\Pi - c\,^3\Sigma^+$, being coupled by spin-orbit (SO) interaction, may provide intermediate levels for efficient absorption-emission cycles (in the Λ scheme) into singlet and triplet ground states for ultracold molecules formation; see [3] for a general analysis. Some promising applications have been recently accomplished for RbCs [9–12], NaCs [13,14], and LiCs [15] dimers. Besides, such systems provide a window to the higher excited triplet states (in a ladder scheme).

Favorably for the above applications, strongly mixed $A\,^1\Sigma^+ - b\,^3\Pi$ complex is formed in alkali-metal diatomic molecules containing the heaviest Cs atom, when the $A\,^1\Sigma^+$ and $b\,^3\Pi$ states may be considered as fully coupled electronic states due to the large value of spin-orbit interaction mainly determined by the Cs $(6\,^2P)$ atom: $\xi_{Cs} = [E_{6\,^2P_{3/2}} - E_{6\,^2P_{1/2}}]/3 = 184.68$ cm^{-1} is the experimental atomic SO parameter [16,17]. The challenging issue lies, however, in the very strong perturbation of the regularity of the rovibrational structure and spectra. Therefore, although the spectra to and/or from the *A*-*b* complex are recorded with the highest possible accuracy of conventional spectroscopy, say within the Doppler width, there is no straightforward recipe for a direct transformation of the available experimental information on term values into the deperturbed structure parameters that would reproduce the empirical spectroscopic data within accuracy of measurements by solving a direct problem. Moreover, as was demonstrated in the recent work on the $A\,^1\Sigma^+ - b\,^3\Pi$ complex of a RbCs dimer [9], even vibrational assignment of the upper rovibronic terms based on the Fourier-transform spectroscopy data remains questionable. There were doubts expressed in Ref. [9] whether it is at all possible to describe a large fraction of the *A*-*b* RbCs spectroscopic data with accuracy better than 0.25 cm^{-1} without accounting for the influence of the higher-lying states. The goal of the present work is to resolve this challenging issue in the NaCs *A*-*b* complex by performing high-resolution spectroscopy studies and applying the adequate data processing to get empirical molecular structure parameters, namely the deperturbed $A\,^1\Sigma^+$ and $b\,^3\Pi$ potential-

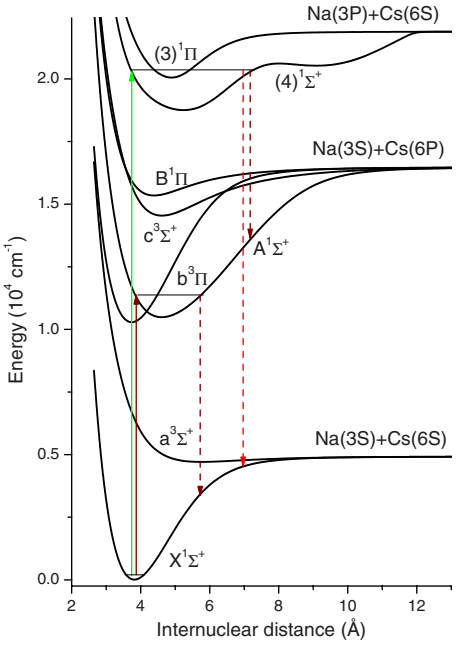

FIG. 1. (Color online) Scheme of the selected lowest electronic states of the NaCs molecule [20] along with the laser excitation and FTS fluorescence observation used in the present experiment.

energy curves (PECs) and relevant spin-orbit interaction matrix elements, that would reproduce the spectroscopy data with experimental accuracy of the order of 0.01 cm^{-1}.

The motivation to choose in the present study the NaCs molecule as a Cs-containing dimer is as follows. Na and Cs cold collisions were studied in a Na+Cs trap [18]; ultracold NaCs molecules were successfully formed and studied in [13,14], followed by a complementary study [7] of the Na+Cs pair interaction based on a conventional spectroscopy method. Regarding necessary ground electronic state data, previous studies [5,7] yielded high-accuracy adiabatic PECs for the lowest $X\ ^1\Sigma^+$ and $a\ ^3\Sigma^+$ states up to their dissociation limit Na(3 ^2S)+Cs(6 ^2S) (Fig. 1). The $B(1)\ ^1\Pi$ state was recently studied as well in Ref. [19], and, hence, the next logical step is to investigate the $A\ ^1\Sigma^+ - b\ ^3\Pi$ complex converging to the same atomic asymptote Na(3 ^2S)+Cs(6 ^2P).

Spectroscopic studies of the *A-b* mixed states in heteronuclear alkali-metal diatomics are greatly facilitated by the recent high-quality electronic-structure calculations performed in pure Hund's coupling cases [26] (*a*) [20–24] and (*c*) [25], respectively. In particular, the recent quasirelativistic calculations of spin-orbit coupling matrix elements between the low-lying NaCs electronic states [22] are found to be a crucial point for making a reliable initial guess on the explicitly *r*-dependent SO interaction parameters of a deperturbation model used. Furthermore, it is suggested in the present work to include the best available *ab initio* PECs and SO matrix elements, when properly weighted, into the nonlinear fitting procedure of the experimental data set in order to regularize the resulting empirical functions at small and large internuclear distances. This, on a more general level, provides a natural step toward closing the gap between the vast majority of good-quality *ab initio* calculations and the extremely scarce and fragmentary amount of empirical data, regarding even low-lying excited electronic states of alkali-metal diatomic molecules.

Regarding the recent experimental studies of the *A-b* mixed states in alkali-metal diatomic molecules by Fourier transform spectroscopy, the investigations in Na_2 [27], K_2 [28], Rb_2 [29,30], Cs_2 [30] and RbCs [9] are to be mentioned. As far as heteronuclear alkali-metal diatomics are concerned, the most comprehensive information was obtained for NaRb [31–33] and the present research is for us a natural next step after the recently performed deperturbation studies of the $A\ ^1\Sigma^+ - b\ ^3\Pi$ complex in the NaRb molecule.

In Ref. [33], 2300 experimental term values of the NaRb $A\ ^1\Sigma^+ - b\ ^3\Pi$ complex were measured using a Fourier transform spectrometer with about 0.01 cm^{-1} accuracy and have been reproduced, for both $Na^{85}Rb$ and $Na^{87}Rb$ isotopomers, with a standard deviation of 0.012 cm^{-1} exploiting a direct deperturbation analysis by means of the inverted channel-coupling approach with Hund's-coupling case (*a*) basis functions. The situation for the $A\ ^1\Sigma^+ - b\ ^3\Pi$ complex in NaCs is, however, much more complicated since the *ab initio* estimate of the SO coupling between the $A\ ^1\Sigma^+$ and $b\ ^3\Pi_{\Omega=0}$ states $\xi^{SO}_{Ab_0}$ [22] is about 90 cm^{-1}, to be compared with the harmonic vibrational frequencies of the virtually isolated $A\ ^1\Sigma^+$ and $b\ ^3\Pi$ states $\omega^A_e \approx 60$ cm^{-1} and $\omega^b_e \approx 100$ cm^{-1} [20], respectively. The adiabaticity parameter $\gamma = \frac{\xi^{SO}_{Ab_0}}{\sqrt{\omega^A_e \omega^b_e}}$, being close to unity, provides the considerable systematic nonadiabatic energy shifts of practically all levels of the complex. Thus, it is hopeless to find out weakly perturbed term values to be used for preliminary diabatic or adiabatic processing corresponding to pure Hund's-coupling cases (*a*) or (*c*), respectively. For a comparison, the characteristic $\xi^{SO}_{Ab_0}$ value of the *A-b* complex in a NaRb dimer [33] is about 2.5 times smaller than in NaCs. This allowed one to observe and to include weakly perturbed levels in the initial steps of analysis in order to obtain the correct *v*-assignment from the intensity distribution in LIF progressions from the $A\ ^1\Sigma^+ - b\ ^3\Pi$ complex in NaRb [31–33].

What is even more important, the natural NaCs sample does not consist of different isotopomers that may facilitate *v*-numbering. Therefore, a main feasible tool to unambiguously confirm the term value deperturbation analysis has to be based only on checking laser induced fluorescence (LIF) intensity distribution (see Refs. [31,32]). It should be stressed, however, that a rigorous vibrational assignment of the strongly mixed $A\ ^1\Sigma^+$ and $b\ ^3\Pi$ states cannot be achieved in principle due to the breakdown of the oscillation theorem [34] for multichannel nonadiabatic states. Thus, a subsequent presented vibrational identification v_A, v_b of the NaCs *A-b* complex relates only to the conventional vibrational quantum numbers of the deperturbed (diabatic) $A\ ^1\Sigma^+$ and $b\ ^3\Pi_{\Omega=0}$ states, respectively.

The paper is structured as follows. A brief description of the experiment as well as the procedure of rovibrational assignment and term values determination of the *A-b* complex is given in Sec. II. The elaborated model Hamiltonian and nonlinear fitting procedure used for a direct deperturbation analysis of term values of the complex are explained in Secs. III A–III D, while the resulting empirical interatomic PECs and SO coupling functions are discussed and compared with

their *ab initio* counterparts in Sec. III E. The estimated nonadiabatic A-b wave functions are used in Sec. IV A to simulate relative intensity distributions in the observed $A-b \rightarrow X$ LIF progressions. The radiative lifetimes of the A-b complex, as well as the wave numbers and probabilities of the pump-dump transitions for the optical conversion cycle $a \rightarrow A-b \rightarrow X$, are predicted in Sec. IV B.

II. FOURIER TRANSFORM SPECTROSCOPY OF THE A-b COMPLEX

A. Experiment

The NaCs molecules were produced in a stainless steel heat pipe similar to the one developed for the NaRb [35,36] and NaCs ground-state [5,7] studies. The heat-pipe was filled with 10 g Na and 5 g Cs (both metals in ampoules from Alfa Aesar). A 5 g ampoule with Cs was loaded into the side container [7] at the central part of the heat pipe. Typical operating pressure of Ar buffer gas was 3–5 mbar. During the experiments, the heat pipe was kept at about 300 °C by a Carbolite furnace.

The laser beam was sent into the heat pipe through a pierced mirror. The backwards LIF was collected by the same mirror and focused, by two lenses, on the input aperture of the Fourier transform spectrometer (FTS) Bruker IFS 125HR. For the (LIF) detection in visible spectral region we used a broadband photomultiplier, while for the infrared light detection we used an InGaAs diode operated at room temperature. In order to suppress the He-Ne laser built in the FTS for path difference calibration, a notch filter was placed in front of the detectors. The resolution of the FTS was typically set to 0.03–0.05 cm^{-1}. In order to ensure a sufficient signal-to-noise ratio for the lines of medium strength, the number of scans for each recorded spectrum varied from 20 to 40; averaging over a number of repeated measurements was applied in some cases.

Two excitation-observation schemes were used for the A-b complex data collection, see Fig. 1, similarly to the NaRb A-b complex studies in Ref. [33]. First, the NaCs molecules were excited by the Ar^+-laser lines 501.7 nm (multimode operation regime) and 514.5 nm (single-mode operation regime). The corresponding LIF series to the A-b complex were measured within the [6000, 12000] cm^{-1} spectral range while the strongest signal was observed in the [7000, 8500] cm^{-1} spectral range. Figure 2(a) represents such a spectrum detected for a particular single mode at 514.5 nm line excitation. It is known from the preceding experiments [5,7,19] that these Ar^+-laser lines excite both (3) $^1\Pi$ and (4) $^1\Sigma^+$ states of the NaCs molecule. However, as was estimated in Ref. [23] by means of the relevant *ab initio* transition dipole moments, the (3) $^1\Pi \rightarrow A-b$ emission is expected to be very weak and can be practically neglected. Hence, the spectrum shown in Fig. 2(a) can be attributed to the (4) $^1\Sigma^+ \rightarrow A-b$ transitions. In order to simplify the assignment of the observed infrared (ir) transitions, LIF spectra to the ground state were also recorded in the visible spectral region at the same excitation conditions, see Fig. 2(b). The transitions around 17 600 cm^{-1} represent the (3) $^1\Pi \rightarrow X\,^1\Sigma^+$ LIF while the transitions around 15 200 cm^{-1} belong to the (4) $^1\Sigma^+ \rightarrow X\,^1\Sigma^+$ LIF.

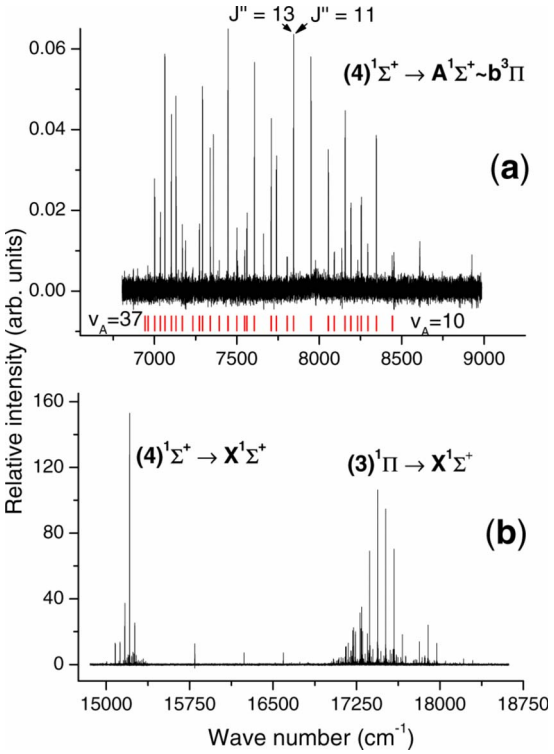

FIG. 2. (Color online) Examples of LIF spectra excited by an Ar^+ 514.5 nm line (single mode). (a) The (4) $^1\Sigma^+(v^*;J'=12) \rightarrow A\,^1\Sigma^+ - b\,^3\Pi(v_A=10-37;J''=11,13)$ LIF progression. Each line represents a narrow doublet with $J''=11$ and 13. Short vertical bars (red) indicate the assigned doublets. (b) The respective spectrum to the ground $X\,^1\Sigma^+$ state at the same excitation. High-frequency region of the spectrum is cut off by a long pass edge filter. The strongest progression from the (4) $^1\Sigma^+$ state is excited in the transition (4) $^1\Sigma^+(v^*;J'=12) \leftarrow X\,^1\Sigma^+(v_X=1;J''=11)$.

Another excitation-observation scheme consisted in a direct excitation of the A-b complex by various diode lasers followed by observation of the $A-b \rightarrow X\,^1\Sigma^+$ LIF, see Fig. 1. Three laser diodes, namely 850 nm (LD850/100 from Toptica Photonics), 980 nm (L980P200I from Thorlabs), and 1020 nm (LD1020/400 from Toptica Photonics), were mounted in homemade external cavity resonators (Littrow configuration), with a grating serving as a feedback source. The respective frequency tuning ranges were [11550, 11940], [10209, 10515], and [9700, 9940] cm^{-1}. Excitation frequencies were measured by a wavemeter HighFinesse WS6 with about 0.015 cm^{-1} accuracy. A fine tuning of the grating was achieved by a piezoelectric actuator. Temperature and current stabilization have been provided by Thorlabs controllers. The power of the lasers at the entrance of the heat pipe varied from 15 to 40 mW depending on a particular laser diode and exploited laser current.

Overall 64 excitation frequencies were exploited with the 850 nm diode. A typical LIF spectrum recorded with this diode excitation is shown in Fig. 3(a). The LIF intensity distribution in such a long progression as depicted in Fig. 3(a) with a last maximum at high v_X is characteristic for

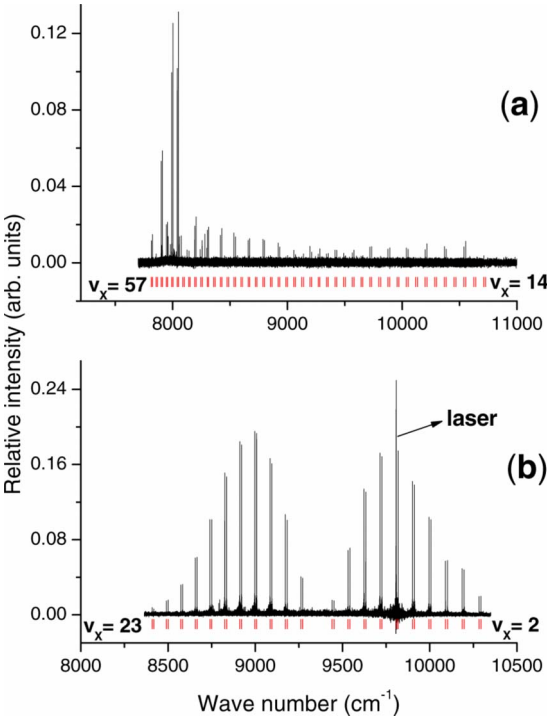

FIG. 3. (Color online) Examples of $A\,^1\Sigma^+ - b\,^3\Pi \rightarrow X\,^1\Sigma^+$ LIF spectra at diode laser excitation. (a) Laser frequency was fixed at 11 906.718 cm^{-1} to excite the $A\,^1\Sigma^+ - b\,^3\Pi(v_A=29; J'=75) \leftarrow X\,^1\Sigma^+(v_X=1; J''=76)$ transition. LIF intensity signal toward the high-frequency region is gradually suppressed because of diminishing spectral sensitivity of the InGaAs detector and by the presence of the long pass edge filter cutting off the transitions above 11 000 cm^{-1}. (b) Laser frequency fixed at 9807.85 cm^{-1} is used to excite the $A\,^1\Sigma^+ - b\,^3\Pi(v_A=1; J'=49) \leftarrow X\,^1\Sigma^+(v_X=7; J''=50)$ transition.

highly excited vibrational levels v_A of the A-b complex. In order to go down in v_A values, a 980 nm diode was used. Unfortunately the relevant LIF signals were found to be very weak if compared to 850 nm diode excitation, and, hence, only a few spectra could be recorded at excitation frequencies around 10 500 cm^{-1}.

The usage of 1020 nm laser diode was more efficient, and a rather strong LIF signal made it possible in a number of cases to detect spectra even without filtering of scattered laser light. Thus, full LIF progressions could be recorded, which was important for establishing vibrational assignment of the upper state. The example of such a full LIF progression recorded for the $v_A=1$ level, with characteristic two maxima in intensity distribution, is given in Fig. 3(b). Overall 37 excitation frequencies within the [9807,9930] cm^{-1} range allowed us to observe about ten vibrational levels of the $A\,^1\Sigma^+$ state starting from the lowest $v_A=0$.

In a number of cases, wide groups of satellite lines appeared around the strong LIF lines due to collision induced distribution of the population of the directly excited rovibronic level over neighboring rotational levels.

B. Spectra analysis

The fully mixed character of the A-b complex leads to strong irregularities in the vibrational and rotational spacings

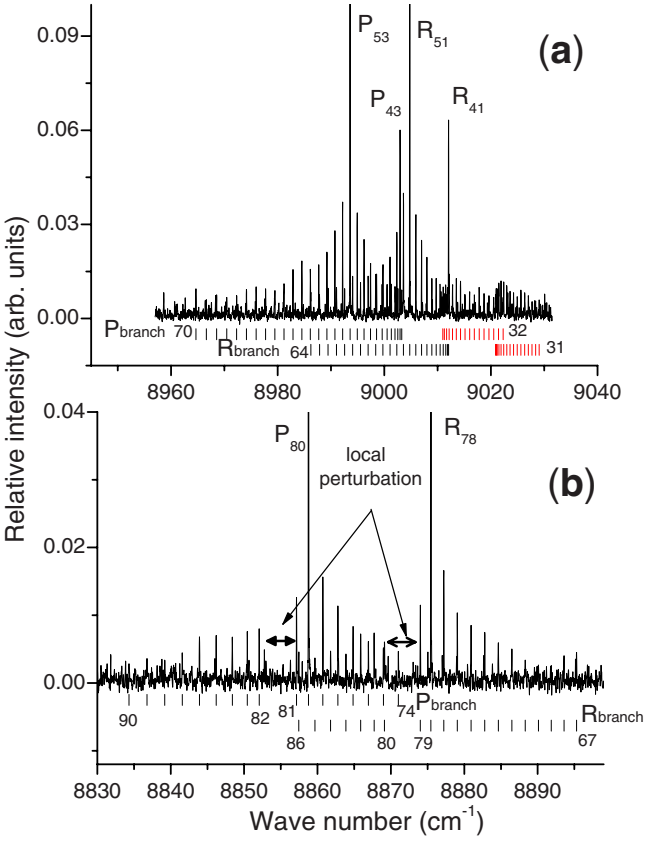

FIG. 4. (Color online) (a) A fragment of the $A\,^1\Sigma^+ - b\,^3\Pi \rightarrow X\,^1\Sigma^+$ LIF spectrum to $v_X=16$ recorded at 9814.967 cm^{-1} diode laser excitation. The excitation transitions are $A\,^1\Sigma^+ - b\,^3\Pi(v_A=1, J'=52) \leftarrow X\,^1\Sigma^+(v_X=7, J''=51)$ and $A\,^1\Sigma^+ - b\,^3\Pi(v_A=1, J'=42) \leftarrow X\,^1\Sigma^+(v_X=7, J''=43)$. The short vertical bars indicate assigned P and R transitions from neighbor collisionally populated A-b rotational levels. Indicated J values correspond to the ground state. (b) A fragment of the $A\,^1\Sigma^+ - b\,^3\Pi \rightarrow X\,^1\Sigma^+$ LIF spectrum to $v_X=17$ recorded at 9855.176 cm^{-1} diode laser excitation. The excitation transition is $A\,^1\Sigma^+ - b\,^3\Pi(v_A=1, J'=79) \leftarrow X\,^1\Sigma^+(v_X=6, J''=78)$.

in this system. Moreover, due to this mixing the transitions to both components (one of mostly singlet character and another one of mostly triplet character) of the complex could be observed simultaneously. Hence, direct rovibrational assignment of the (4) $^1\Sigma^+ \rightarrow A\,^1\Sigma^+ - b\,^3\Pi$ transitions is ambiguous, if at all possible, without a preceding detailed knowledge of the rovibrational levels position in the A-b complex.

Thus, the $A\,^1\Sigma^+ - b\,^3\Pi \rightarrow X\,^1\Sigma^+$ LIF spectra have been analyzed first, since progressions could be easily assigned because of a very accurate ground $X\,^1\Sigma^+$ state PEC [5]. The term values of the A-b complex were obtained by adding the corresponding ground-state rovibronic level energy to a transition wave number. The data field of the A-b complex term values was substantially enlarged after analysis of the satellite lines appearing due to collision induced rotational relaxation; see, for instance, Fig. 4. Due to a rich rotational relaxation, in some spectra both mixed singlet and triplet states were simultaneously observed. Figure 4(a) represents such a situation when an initial population of the optically excited levels $v_A=1; J'=42$ and $v_A=1; J'=52$ is collisionally distributed within two mixed rotational level manifolds. In addition

to the relaxation lines surrounding the strong central P, R lines originating from the directly excited levels with $J'=52$ and 42, two groups of weaker lines around 9020 cm^{-1} can be easily seen. The assigned relaxation lines are marked with black and red vertical bars, respectively. These weak groups of P, R branches without clear central lines are originating from the collisionally excited rotational levels just in the region of a strong local perturbation. Figure 4(b) gives an example of a weak local perturbation observed for the same $v_A=1$ vibrational level at higher rotational levels with the perturbation center at $J_A=80/81$. This local perturbation can be clearly recognized from the two gaps ("windows") in the P, R branches. It should be noted that in most recorded spectra the laser excited the levels with a dominant singlet character. However, an opposite situation was observed in some cases, namely optical excitation of a predominantly triplet state level. The main body of the A-b rovibronic levels assigned from the rovibronic $A\ ^1\Sigma^+-b\ ^3\Pi \rightarrow X\ ^1\Sigma^+$ transitions covers the range $v_A \in [0,35]$ and $J \in [5,151]$.

Detailed information about rovibronic structure of the A-b complex, derived from the analysis of the $A-b \rightarrow X$ transitions, ensures unambiguous assignment of the (4) $^1\Sigma^+ \rightarrow A$-b LIF transitions with the help of simultaneously recorded (4) $^1\Sigma^+ \rightarrow X\ ^1\Sigma^+$ transitions. The energies of the A-b complex levels were calculated using the wave numbers of the assigned (4) $^1\Sigma^+ \rightarrow A-b$ transitions combined with the respective experimental (4) $^1\Sigma^+$ rovibronic term values. The collisionally induced rotational satellites, when observed, were analyzed in these spectra as well, providing additional rotational term values of the A-b complex. In total, two (4) $^1\Sigma^+ \rightarrow A-b$ LIF progressions with 514.5 nm line excitation and one progression with 501.7 nm line excitation have been recorded and assigned.

Summarizing, the FTS analysis of the (4) $^1\Sigma^+ \rightarrow A\ ^1\Sigma^+-b\ ^3\Pi$ and $A\ ^1\Sigma^+-b\ ^3\Pi \rightarrow X\ ^1\Sigma^+$ LIF spectra provided overall about 1160 term values assigned to the e-symmetry rovibronic levels of the $A\ ^1\Sigma^+-b\ ^3\Pi$ complex. The resulting data field depicted in Fig. 5 and presented numerically in the EPAPS tables [37] covers the rotational quantum number range $J \in [5,151]$ and the energy range $E \in [10577,13668]$ cm^{-1} of the A-b complex, including the lowest vibrational level $v_A=0$ of the singlet state. The main contribution to the uncertainty of the experimental term values is given by the Doppler broadening of the absorption transition in the NaCs molecule at working temperatures, its full width at half-maximum (FWHM) being about 0.03 cm^{-1} in the visible spectral region, while diminishing to about 0.01 cm^{-1} in the spectral region around 8000 cm^{-1}. A possible excitation frequency shift from the center of the absorbtion transition yields the respective shift in LIF transitions, thus we conservatively estimate here the term values uncertainty as 0.010–0.015 cm^{-1}. Indeed, a detailed inspection of the individual term values derived from different spectra confirms that their dispersion does not exceed 0.01 cm^{-1}.

For several of the observed $A\ ^1\Sigma^+-b\ ^3\Pi \rightarrow X\ ^1\Sigma^+(v_X)$ LIF progressions, the relative intensity distribution has been analyzed. Taking into account the spectral sensitivity of the InGaAs detector and the spectral transmission of the long pass edge filters, the overall uncertainty of the intensity distribution measurements could be roughly estimated as 15–20 %.

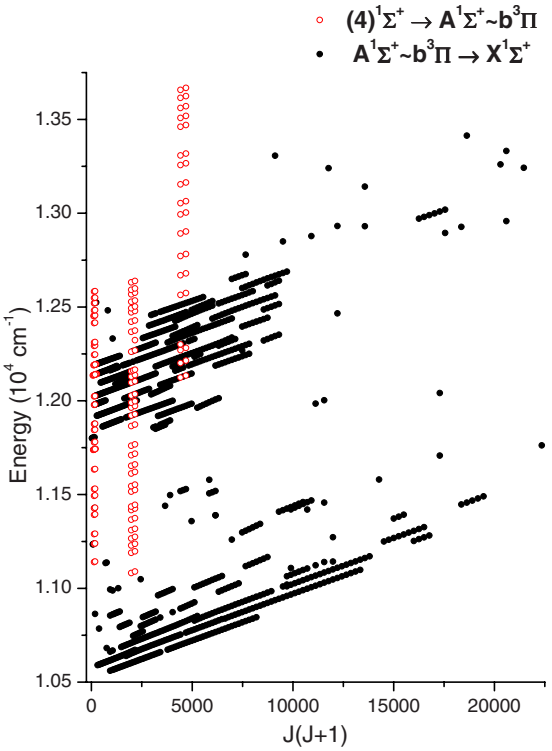

FIG. 5. (Color online) The resulting experimental data field of A-b term values as dependent on $J(J+1)$. Three double columns of the open (red) circles represent the data from the (4) $^1\Sigma^+ \rightarrow A\ ^1\Sigma^+-b\ ^3\Pi$ LIF progressions while the remaining data are derived from the $A\ ^1\Sigma^+-b\ ^3\Pi \rightarrow X\ ^1\Sigma^+$ LIF spectra.

Although the non-Hönl-London factor behavior of intensities in the P and R lines was observed for some strongly perturbed progressions, these intensity anomalies are not pronounced enough to be quantitatively analyzed, since they are comparable with experimental errors.

III. DEPERTURBATION ANALYSIS OF THE TERM VALUES OF A-b COMPLEX

Direct deperturbation analysis of the experimental term values obtained above has been accomplished in the framework of the inverted channel-coupling approach [31,33,38], which is outlined as follows.

The total nonadiabatic rovibronic wave function Ψ^{CC} of the $A\ ^1\Sigma^+-b\ ^3\Pi$ complex with the fixed quantum number J and well-defined e-symmetry is approximated by a linear combination of the symmetrized electronic-rotational wave functions φ_i belonging to a pure Hund's coupling case (a) [26] as $\Psi^{CC}=\Sigma_{i=1}^{M} c_i \varphi_i$, where M is the number of coupled channels (e.g., electronic substates) explicitly involved into consideration; $c_i(r)$ are the fractional components of the total nonadiabatic vibrational wave function $\Phi^{CC}(r)$, which is determined by a solution of the close-coupling radial equations on the infinite interval of the internuclear distance $r \in]0,\infty)$,

$$\left(-\mathbf{I}\frac{\hbar^2 d^2}{2\mu dr^2}+\mathbf{V}(r;\mu,J)-\mathbf{I}E^{CC}\right)\Phi^{CC}(r)=\mathbf{0}, \qquad (1)$$

$$c_i(0) = c_i(\infty) = 0, \tag{2}$$

$$P_i = \int_0^\infty c_i^2(r)dr, \quad \sum_{i=1}^{M} P_i = 1. \tag{3}$$

Here $\mathbf{I}$ is the identity matrix, E^{CC} is the total nonadiabatic energy of the rovibronic level of the complex, while $\mathbf{V}$ is the symmetric $M \times M$ matrix of potential energy explicitly depending on reduced mass μ and rotational quantum number J as a parameter. P_i is the fractional partition of a nonadiabatic wave function.

A. Reduced 2×2 Hamiltonian

The simplest deperturbation model appropriate to the present complex explicitly takes into account only the direct strong spin-orbit interaction between the singlet A state and the $\Omega=0$ component of the triplet b state: $\Psi^{CC}=c_A\varphi_A + c_{b_0}\varphi_{b_0}$. The relevant symmetric 2×2 matrix of potential energy $\mathbf{V}$ has the form [39]

$$V_{^1\Sigma^+} = U_A + B[X+2], \tag{4}$$

$$V_{^3\Pi_0} = U_{b_0} + B[X+2], \tag{5}$$

$$V_{^1\Sigma^+-{}^3\Pi_0} = -\sqrt{2}\xi^{SO}_{Ab_0}, \tag{6}$$

where

$$B \equiv \frac{\hbar^2}{2\mu r^2}, \quad X \equiv J(J+1), \tag{7}$$

while $U_A(r), U_{b_0}(r)$ are the diabatic PECs of the mutually perturbed states and $\xi^{SO}_{Ab_0}(r)$ is the relevant SO coupling matrix element. Hereafter, all electronic parameters of the deperturbation model used are assumed to be mass-invariant. According to van Vleck's pure precession hypothesis [26], the rotational part of the Hamiltonian was evaluated assuming that the diagonal angular momentum matrix elements $L(L+1)=2$ for all states of the p-complex. The validity of the pure precession hypothesis for the $A\ ^1\Sigma^+$ and $b\ ^3\Pi$ states of NaCs has been justified by the *ab initio* calculations of the L-uncoupling matrix elements between singlet $B\ ^1\Pi - A\ ^1\Sigma^+$ and triplet $b\ ^3\Pi - a\ ^3\Sigma^+$ interacting pairs performed in [22,40] since both $L_{BA}(R)$ and $L_{ba}(R)$ functions were found to be very close to the pure precession value $\sqrt{2}$ at small and intermediate internuclear distances.

B. Conventional 4×4 Hamiltonian

High rotational levels of the complex available from the present experiment ($J \leqslant 151$) require, however, an explicit treatment of the pronounced spin-rotational interaction between different Ω components of the triplet $b^3\Pi_\Omega$ state as well [26]. It immediately leads to a more complicated four-channels problem $\Psi^{CC}=\sum_{i=1}^{M=4} c_i\varphi_i$, where $i \in [A\ ^1\Sigma^+, b\ ^3\Pi_{\Omega=0,1,2}]$ and the corresponding 4×4 $\mathbf{V}$ matrix has the additional, in comparison with the simplest 2×2 model (Sec. III A), nonvanishing matrix elements [39],

$$V_{^3\Pi_1} = U_{b_0} + A^{SO} + B[X+2], \tag{8}$$

$$V_{^3\Pi_2} = U_{b_0} + 2A^{SO} + B[X-2], \tag{9}$$

$$V_{^3\Pi_0-{}^3\Pi_1} = -B\sqrt{2X}, \tag{10}$$

$$V_{^3\Pi_1-{}^3\Pi_2} = -B\sqrt{2(X-2)}. \tag{11}$$

Here $A^{SO}(r)$ is assumed to be the equidistant splitting between the $\Omega=0,1,2$ components of the triplet state.

C. Elaborated 4×4 model

In order to account for regular spin-orbit and electronic-rotational perturbations caused by the remote $^1\Pi$ and $^3\Sigma^+$ states manifold (first of all the nearest $B\ ^1\Pi$ and $c\ ^3\Sigma^+$ states converging to the same dissociation limit, see Fig. 1), the nonequidistant SO splitting between the $b\ ^3\Pi_{\Omega=0,1,2}$ components $[A^{SO}_{01}(r) \neq A^{SO}_{12}(r)]$,

$$V_{^3\Pi_1} = U_{b_0} + A^{SO}_{01} + B[X+2], \tag{12}$$

$$V_{^3\Pi_2} = U_{b_0} + A^{SO}_{01} + A^{SO}_{12} + B[X-2], \tag{13}$$

and the indirect SO coupling $A\ ^1\Sigma^+ - b\ ^3\Pi_{\Omega=1}$ matrix element $\xi^{SO}_{Ab_1}(r)$,

$$V_{^1\Sigma^+-{}^3\Pi_1} = -B\sqrt{2X}\xi^{SO}_{Ab_1}, \tag{14}$$

were incorporated into the conventional 4×4 Hamiltonian (Sec. III B). These phenomenologically introduced matrix elements appear due to the second-order contact transformations implicitly performed on the initially full electronic Hamiltonian of infinite dimension ($M \to \infty$). Thus, the diabatic PECs $U_A(r)$, $U_{b_0}(r)$ of the interacting $A\ ^1\Sigma^+$ and $b\ ^3\Pi_0$ states, spin-orbit functions $A^{SO}_{01}(r)$, $A^{SO}_{12}(r)$, $\xi^{SO}_{Ab_0}(r)$, and the r-independent matrix element $\xi^{SO}_{Ab_1}$ are the adjustable fitting parameters of the elaborated deperturbation model.

D. Fitting procedure

The required PECs $U_A(r)$ and $U_{b_0}(r)$ of the interacting states were analytically represented by the expanded Morse oscillator (EMO) function [41],

$$U^{EMO}(r) = [T_{dis} - \mathfrak{D}_e] + \mathfrak{D}_e[1 - e^{-\alpha(r)(r-r_e)}]^2, \tag{15}$$

where T_{dis} is the dissociation limit referred to the minimum of the ground state, $\mathfrak{D}_e$ is the well depth, r_e is the equilibrium distance, and α is the polynomial function of the reduced variable $y_p \in]-1,1]$,

$$\alpha(r) = \sum_{i=0}^{m} a_i y_p^i, \quad y_p(r, r_{ref}) = \frac{r^p - r^p_{ref}}{r^p + r^p_{ref}}. \tag{16}$$

The diagonal $A^{SO}_{01}(r)$, $A^{SO}_{12}(r)$, and the off-diagonal $\xi^{SO}_{Ab_0}(r)$, spin-orbit functions were also represented by the appropriate EMO function $V^{EMO}(r)$ converging to the correct atomic limit,

$$V^{\mathrm{EMO}}(r) = [\xi_{\mathrm{Cs}} - V_e] + V_e[1 - e^{-\alpha(r)(r-r_e)}]^2, \qquad (17)$$

since the relevant *ab intio* spin-orbit functions $A^{\mathrm{SO}}(r)$ and $\xi^{\mathrm{SO}}_{Ab_0}(r)$ clearly demonstrate the Morse-like behavior [22].

The initial parameters of the above EMO functions (15) and (17) were evaluated in the framework of the weighted nonlinear least-squares fitting (NLSF) procedure [42],

$$\chi^2_{ab} = \sum_{j=1}^{N_{ab}} \frac{[U^{\mathrm{EMO}}(r_j) - U^{ab}(r_j)]^2}{(\sigma^{ab}_j)^2[N_{ab} - m_p]}, \qquad (18)$$

exploiting the *ab initio* PECs U^{ab}_A, U^{ab}_b and SO functions $A^{\mathrm{SO}}, \xi^{\mathrm{SO}}_{Ab_0}$ corresponding to the pure Hund's coupling case (*a*) [20–22]. Here N_{ab} is the number of used *ab initio* r_j points while m_p is the number of fitting parameters. The *ab initio* PECs of the $A\ ^1\Sigma^+$ and $b\ ^3\Pi$ states and their uncertainty σ^{ab}_j were estimated by averaging the independent results of Refs. [20–22], while the σ^{ab}_j values of the $A^{\mathrm{SO}}(r)$ and $\xi^{\mathrm{SO}}_{Ab_0}(r)$ functions borrowed from Ref. [22] were assumed not to exceed 15% of the relevant *ab initio* values.

Then, the refined parameters of the required U_A, U_{b0}, A^{SO}_{01}, A^{SO}_{12}, $\xi^{\mathrm{SO}}_{Ab_0}$ functions combined with the single *r*-independent parameter $\xi^{\mathrm{SO}}_{Ab_1}(r)$=const were determined iteratively during the weighted NLSF procedure [26],

$$\chi^2_{\mathrm{expt}} = \sum_{j=1}^{N_{\mathrm{expt}}} \frac{w_j(E^{\mathrm{CC}}_j - E^{\mathrm{expt}}_j)^2}{N_{\mathrm{expt}} - M_p}, \qquad (19)$$

where $w_j = 1/\sigma^2_j$ is the weight of each level, E^{expt}_j is the experimental term value, and σ_j=0.010–0.015 cm^{-1} represents its uncertainty. Here, N_{expt} is the number of experimental term values while M_p is the total number of adjusted fitting parameters of the deperturbation model used. The robust weighting procedure [43] $w_j = 1/(\sigma^2_j + \delta^2_j/3)$ was used at the initial stages of the fitting process to diminish an undesirable effect of strongly perturbed and/or incorrectly assigned lines; $\delta_j = E^{\mathrm{CC}}_j - E^{\mathrm{expt}}_j$ is the deviation observed in the preceding fit iteration.

During the final stages of the NLSF procedure, the experimental data set was extended by the corresponding *ab initio* PEC and SO points outside the experimental region to regularize the resulting EMO function behavior at small and large internuclear distances. The minimum of a sum of the relevant χ^2_{ab} (18) and χ^2_{expt} (19) functions was searched by the modified Levenberg-Marquardt algorithm [44] realized in MINPACK software [45]. The required partial derivatives of the eigenvalues E^{CC}_j with respect to the fitting parameters a_i were evaluated by means of the diagonal Hellmann-Feynman theorem [26]: $\partial E^{\mathrm{CC}}/\partial a_i = \langle \mathbf{\Phi}^{\mathrm{CC}} | \partial \mathbf{V}/\partial a_i | \mathbf{\Phi}^{\mathrm{CC}} \rangle$.

The analytical two-parameter mapping procedure [46] based on replacement of the usual integration variable $r \in [0,\infty)$ by the reduced radial variable $y(r;\bar{r}=4.6,\alpha=5.2) = 1/[1+(\bar{r}/r)^{\alpha}]$; $y \in [0,1]$ was used to transform the initial CC equations (1) into completely equivalent form. Then, the modified CC equations given explicitly in Ref. [33] were efficiently solved by the ordinary finite-difference (FD) boundary value method [47] using the central five-point FD approximation of the kinetic-energy term. The ordinary eigenvalue and eigenfunction problem of the resulting symmetric band matrix was iteratively solved by the implicitly restarted Lanczos method realized in ARPACK software [48] in the shift-inverted spectral transformation mode.

E. Resulting interatomic potentials and spin-orbit functions

Overall 26 EMO fitting parameters corresponding to the diabatic PECs $U_A\ ^1\Sigma^+$, $U_b\ ^3\Pi_0$, and the off-diagonal SO coupling function $\xi^{\mathrm{SO}}_{Ab_0}$ of the simplest 2×2 deperturbation model (Sec. III A) were required to reproduce about 70% experimental term values of the *A*-*b* complex with a standard deviation of 0.008 cm^{-1}, which is quite comparable with the estimated uncertainty of the FTS measurements. As expected, the most significant deviations are observed for the highest rotational levels of the complex where a spin-rotational interaction becomes very important [26].

Application of the conventional 4×4 deperturbation model (Sec. III B) determined by overall 28 molecular parameters belonging to the EMO fitting $U_A\ ^1\Sigma^+$, $U_b\ ^3\Pi_0$, $\xi^{\mathrm{SO}}_{Ab_0}$, and A^{SO} functions improves the fitting quality significantly and reproduces almost 97% experimental term values with a standard deviation of 0.006 cm^{-1}. Furthermore, a phenomenological account for remaining regular perturbations caused by remote states in the framework of the elaborated deperturbation model (Sec. III C) particularly improves a reproduction of rovibronic term values having significant admixture of the $b\ ^3\Pi_{\Omega=1}$ component. The resulting 31 molecular parameters of the elaborated model (Sec. III C given in Tables I and II, and EPAPS [37] completely define the empirical diabatic PECs $U_A\ ^1\Sigma^+$, $U_b\ ^3\Pi_0$ of the mutually perturbed states, as well as the spin-orbit coupling functions A^{SO}_{01}, A^{SO}_{12}, $\xi^{\mathrm{SO}}_{Ab_0}$, and $\xi^{\mathrm{SO}}_{Ab_1}$, reproducing 98% of the experimental term values with a standard deviation of 0.006 cm^{-1}. For comparison with *ab initio* calculations [20–22], diabatic $A\ ^1\Sigma^+$ and $b\ ^3\Pi_1$ components (defined as $U_{b_1} = U_{b_0} + A^{\mathrm{SO}}_{01}$) are plotted in Fig. 6(a), while the respective SO functions are presented in Fig. 7. Besides the experimental and reproduced rovibronic levels of the *A*-*b* complex, the EPAPS tables also contain the fractional partition P_i of the nonadiabatic wave functions. This fractional analysis confirmed the expected strong singlet-triplet mixing effect between the $A\ ^1\Sigma^+$ state and the $b\ ^3\Pi_{\Omega=0}$ component for the majority of observed levels of the complex, while only 2% of the experimental data highlighted a significant admixture of the $b\ ^3\Pi_{\Omega=1}$ component.

Figure 7 clearly demonstrates the Morse-like behavior of both SO splitting $A^{\mathrm{SO}}(r)$ and SO coupling $\xi^{\mathrm{SO}}_{Ab_0}$ functions. A single minimum of these functions observed at $r \approx 4.5$ Å reaches 80 cm^{-1}. This is almost 2.5 times less than the respective SO Cs atom parameter $\xi^{\mathrm{SO}}_{\mathrm{Cs}(6\ ^2P)} = 184.67\ \mathrm{cm}^{-1}$ and it is almost 14 times larger than the Na atom SO parameter $\xi^{\mathrm{SO}}_{\mathrm{Na}(3\ ^2P)} = 5.73\ \mathrm{cm}^{-1}$. This unexpectedly strong *r* dependence of the derived SO functions seems to be attributed to the pronounced fractional mixing of the singly occupied $p\pi$ and $p\sigma$ molecular orbitals built from both Na and Cs atoms having significantly different strength of SO interaction in their lowest ^2P states.

TABLE I. The resulting EMO parameters of the diabatic potential-energy curves of the deperturbed $A\,^1\Sigma^+$ and $b\,^3\Pi_0$ states. The fixed parameter $^\dagger p=3$ is used for both states. The fixed $^\dagger T^A_{\rm dis}=D^X_e+\Delta E_{\rm Cs}-\xi_{\rm Cs}$ and $^\dagger T^{b_0}_{\rm dis}=T^A_{\rm dis}-\xi_{\rm Cs}$ values were calculated from the ground-state well-depth $D^X_e=4954.24$ cm^{-1} [7], the experimental SO parameter of the Cs atom in the $6\,^2P$ state $^\dagger\xi_{\rm Cs}=184.68$ cm^{-1} [16,17], and experimental transition energy (without hfs splitting) $\Delta E_{\rm Cs}=11\,732.31$ cm^{-1} of the Cs atom $6\,^2P_{3/2}-6\,^2S_{1/2}$ transition [16]. It should be noted that the only reason for the large number of digits in r_e and a_i is to ensure the reproducibility of the fit. The same reason is applied to $\xi^{\rm SO}_{Ab_1}$ in Table II. Numbers in brackets are the power to base 10 of the associated number. Daggers denoted fixed parameter.

	$A\,^1\Sigma^+$	$b\,^3\Pi_0$
$^\dagger T_{\rm dis}$ (cm^{-1})	16501.87	16317.19
$^\dagger r_{\rm ref}$ (Å)	4.65	3.78
T_e (cm^{-1})	10509.810	10236.048
$\mathfrak{D}_e$ (cm^{-1})	5992.060	6081.142
r_e (Å)	4.65431678872284	3.77999922692013
a_0 (Å^{-1})	0.4092019271344[0]	0.665282316447219[0]
a_1 (Å^{-1})	−0.316930094322587[−1]	0.159655197110690[0]
a_2 (Å^{-1})	0.118889237998245[0]	0.144813242483051[0]
a_3 (Å^{-1})	0.272082736776197[0]	0.964993864916689[−1]
a_4 (Å^{-1})	0.206826824112031[0]	−0.452724688520158[−2]
a_5 (Å^{-1})	−0.147778977004416[0]	0.320383473138789[0]
a_6 (Å^{-1})	−0.491933649692577[0]	0.148834980740537[1]
a_7 (Å^{-1})	0.288158643376113[−2]	−0.180900998067171[1]
a_8 (Å^{-1})	0.839886790201783[0]	−0.388373323943793[0]
a_9 (Å^{-1})	0.358215463426036[0]	

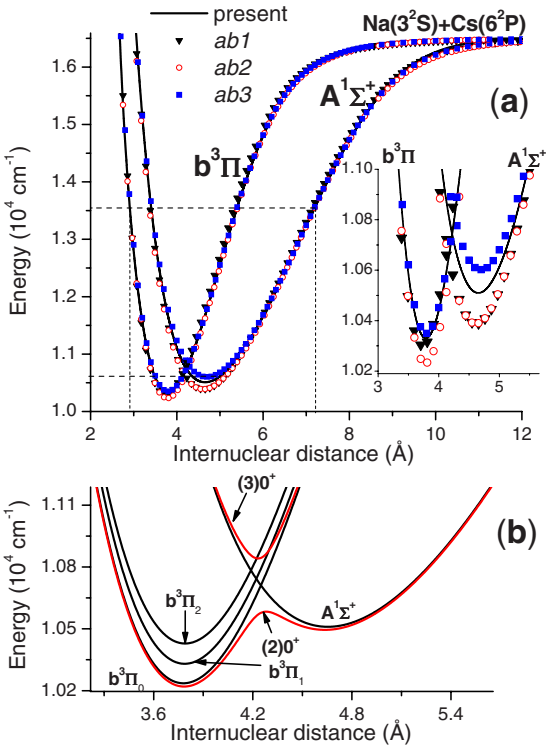

FIG. 6. (Color online) (a) The present empirical and available *ab initio* (*ab*1-[20]; *ab*2-[21]; *ab*3-[22]) PECs for the $A\,^1\Sigma^+$ and $b\,^3\Pi_{\Omega=1}$ states corresponding to Hund's coupling case (*a*). Dashed horizontal and vertical lines indicate the experimentally studied region. The inset shows in the PECs around r_e of the $A\,^1\Sigma^+$ and $b\,^3\Pi$ states. (b) The present diabatic PECs around r_e of the $A\,^1\Sigma^+$, $b\,^3\Pi_{\Omega=0,1,2}$ substates and their adiabatic counterparts $(2,3)\Omega=0^+$ corresponding to Hund's coupling case (*c*).

Both diagonal and off-diagonal SO functions are apparently sensitive to the present experimental data set only in a rather small *r*-region (see Fig. 6). Indeed, since the interacting states cross each other in the single point, the respective vibronic perturbation matrix elements are mainly determined by the SO value near the crossing point, which almost coincides with the stationary phase point [34]. Therefore, the relevant spin-orbit EMO functions (17) were constrained by fixing a_i parameters in Eq. (16) determined from a fit to the *ab initio* points [22], so only V_e and r_e were the free parameters in the global fit (see Table II). In Fig. 6(b), the diabatic PECs are given in the vicinity of r_e ($U_{b_1}=U_{b_0}+A^{\rm SO}_{01}$ and $U_{b_2}=U_{b_1}+A^{\rm SO}_{12}$) together with the avoided crossing adiabatic PECs $U^{\rm ad}_{(2,3)0^+}$, which were estimated from diabatic counterpart $b\,^3\Pi_{\Omega=0}$ and $A\,^1\Sigma^+$ states as

$$U^{\rm ad}_{(2,3)0^+}=[(U_A+U_{b_0})\pm\sqrt{(U_A-U_{b_0})^2+8(\xi^{\rm SO}_{Ab_0})^2}]/2. \tag{20}$$

The resulting empirical PECs and SO matrix elements are found to be very close to their *ab initio* quasirelativistic counterparts [20–22] both inside and outside the experimental data region $r\in[2.9,7.2]$ Å [see Figs. 6(a) and 7]. In particular, a difference of empirical and *ab initio* PECs observed for the $b\,^3\Pi_{\Omega=1}$ and $A\,^1\Sigma^+$ states near their equilibrium distances is about one ($\Delta U_b=80-120$ cm$^{-1}\approx\omega^b_e$) and two ($\Delta U_A=100-130$ cm$^{-1}\approx 2\omega^A_e$) vibrational quanta, respectively; see the inset in Fig. 6(a). Furthermore, the derived empirical splitting of the triplet $b\,^3\Pi$ state $\Delta U_{b_{01}}=109$ and $\Delta U_{b_{12}}=99$ cm^{-1} near the equilibrium distance $r^b_e=3.78$ Å

TABLE II. The resulting EMO parameters of diagonal $A^{\rm SO}_{01}$, $A^{\rm SO}_{12}$, and off-diagonal $\xi^{\rm SO}_{Ab_0}$ spin-orbit coupling functions. The parameters $^\dagger p=1$ and $^\dagger\xi_{\rm Cs}=184.68$ cm^{-1} [16,17] are the same for all SO functions. The empirical *r*-independent indirect SO coupling matrix element $\xi^{\rm SO}_{Ab_1}=0.129\,470\,305\,169\,498$ cm^{-1}. Daggers denote fixed parameter.

Parameter	$\xi^{\rm SO}_{Ab_0}$	$A^{\rm SO}_{01}$	$A^{\rm SO}_{12}$
V_e (cm^{-1})	95.88	108.41	90.88
r_e (Å)	4.851716	4.652394	4.399871
$^\dagger r_{\rm ref}$ (Å)	4.8	4.6	
$^\dagger a_0$ (Å^{-1})	0.34334	0.48369	
$^\dagger a_1$ (Å^{-1})	−0.29306	1.13622	
$^\dagger a_2$ (Å^{-1})	−1.31449	2.67951	
$^\dagger a_3$ (Å^{-1})	5.67884	3.34248	
$^\dagger a_4$ (Å^{-1})	14.01202		

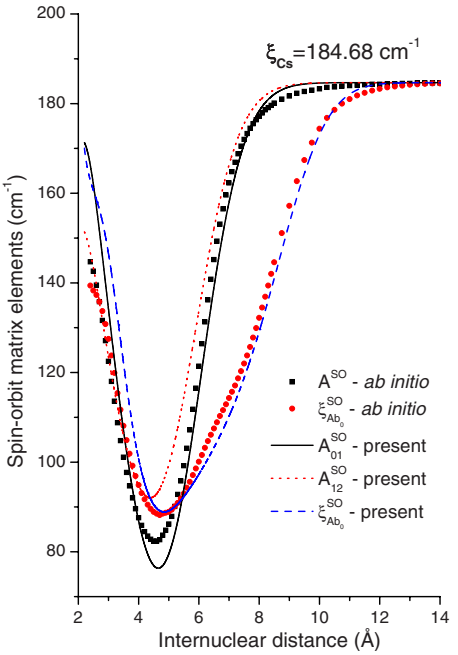

FIG. 7. (Color online) The present empirical and relevant *ab initio* spin-orbit matrix elements from Ref. [22].

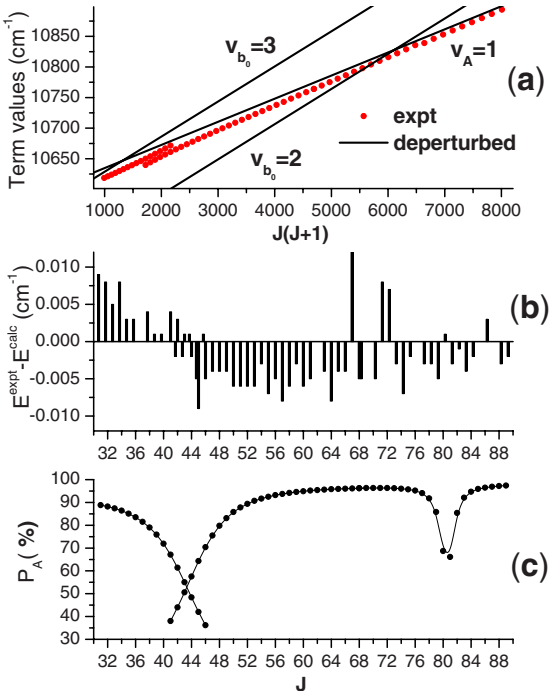

FIG. 8. (Color online) (a) Experimental term values (red filled circles) of the *A*-*b* complex obtained by processing two fragments of the $A\,^1\Sigma^+ - b\,^3\Pi \rightarrow X\,^1\Sigma^+$ LIF spectra presented in Fig. 4. Straight lines correspond to the virtual rovibronic energy of the deperturbed diabatic $A\,^1\Sigma^+$ and $b\,^3\Pi_0$ states. (b) Residuals of the fit for the respective J values. (c) Fractional part of the singlet A state predicted for the observed levels.

[see Fig. 6(b)] agrees well with their *ab initio* counterparts (103 and 91 cm^{-1}, respectively) obtained in the framework of Hund's coupling case (*c*) in Ref. [25].

Figure 8 demonstrates a particular result of the fitting procedure obtained for the term values corresponding to the fragments of the $A-b \rightarrow X\,^1\Sigma^+$ LIF spectra in Fig. 4. The high quality of the fit is illustrated in Fig. 8(b). The averaged residuals of the fit are about 0.005 cm^{-1}. The experimental rovibronic term values presented in Fig. 8(a) basically correspond to the $v_A=1$ vibrational level of the singlet state, which is locally perturbed by the diabatic $v_{b_0}=3$ and 2 levels of the triplet state near $J=44$ and 81, respectively. Additionally, the rovibronic term values of both states undergo regular perturbations leading to a systematic energy shift of the order of 8–12 cm^{-1} even when an admixture of the triplet component does not exceed 5–10 %, as follows from a fraction analysis of the relevant nonadiabatic wave functions; see Fig. 8(c). Moreover, a large off-diagonal SO matrix element $\xi^{SO}_{Ab_0}(r_c) \approx 95$ cm^{-1} near the crossing point $r_c \approx 4.25$ Å of the diabatic $A\,^1\Sigma^+$ and $b\,^3\Pi_{\Omega=0}$ states provides the pronounced nonadiabatic energy shift for practically all levels of the *A*-*b* complex, even when an admixture of the perturbing state is rather small. For example, only 2% admixture of the $b\,^3\Pi_{\Omega=0}$-component for the lowest observed $v_A=0$ level results in ~12–15 cm^{-1} systematic shifts.

IV. RADIATIVE PROPERTIES OF THE $A\,^1\Sigma^+ - b\,^3\Pi$ COMPLEX

The radiative properties of the $A\,^1\Sigma^+ - b\,^3\Pi$ complex can be estimated as well by means of the corresponding nonadiabatic vibrational wave functions Φ^{CC} and available *ab initio* $A\,^1\Sigma^+ - X\,^1\Sigma^+$ and $b\,^3\Pi - a\,^3\Sigma^+$ transition dipole moments $d_{AX}(r)$ and $d_{ba}(r)$ [21,22]. Indeed, since singlet-triplet electric dipole transitions are strictly forbidden in a pure Hund's coupling case (*a*), the required transition moments $M_{A-b\rightarrow X}$ and $M_{A-b\rightarrow a}$ between the $A\,^1\Sigma^+ - b\,^3\Pi$ complex and the low-lying isolated $X\,^1\Sigma^+$ and $a\,^3\Sigma^+$ states (see Fig. 1) are defined as

$$M_{A-b\rightarrow X} = \langle c_A | d_{AX} | v_X \rangle S^{\Omega'\Omega''}_{J'J''}, \tag{21}$$

$$M_{A-b\rightarrow a} = \langle c_{b_\Omega} | d_{ba} | v_a \rangle S^{\Omega'\Omega''}_{J'J''}, \tag{22}$$

where $S^{\Omega'\Omega''}_{J'J''}$ is the analytically known overlap integral between rotational wave functions [26]. The $|c_A\rangle$ and $|c_{b_\Omega}\rangle$ are the respective $A\,^1\Sigma^+$ and $b\,^3\Pi_{\Omega'=0,1,2}$ fractions of the nonadiabatic vibrational wave function of the *A*-*b* complex, while $|v_X\rangle$ and $|v_a\rangle$ are the adiabatic eigenfunctions of the $X\,^1\Sigma^+$ and $a\,^3\Sigma^+$ states, respectively.

A. Intensity distribution in the $A\,^1\Sigma^+ - b\,^3\Pi \rightarrow X\,^1\Sigma^+$ LIF spectra

Relative intensity distributions in a band structure of the measured $A\,^1\Sigma^+ - b\,^3\Pi(J') \rightarrow X\,^1\Sigma^+(v_X;J'')$ LIF progressions were simulated for both weakly and strongly perturbed levels of the complex in order to confirm the reliability of the energy-based deperturbation analysis. Indeed, oscillation of intensities observed in the long LIF series proved to be very sensitive to a specific nodal structure of the perturbed wave

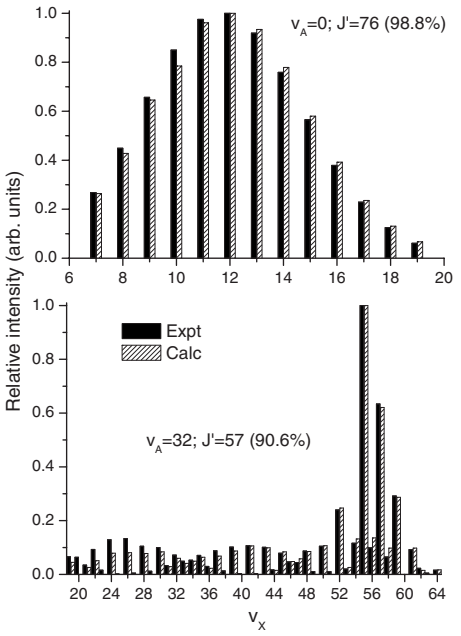

FIG. 9. The calculated and experimental relative intensity distributions in the long $A\,^1\Sigma^+ - b\,^3\Pi \rightarrow X\,^1\Sigma^+(v_X)$ LIF progressions originating from regularly perturbed rovibronic levels $v_A=0$ and 32 of the A-b complex. The number in parentheses denotes the estimated fraction (in percent) of the singlet A state. The intensities of the P and R lines are averaged and normalized to the most intensive transition of the progression.

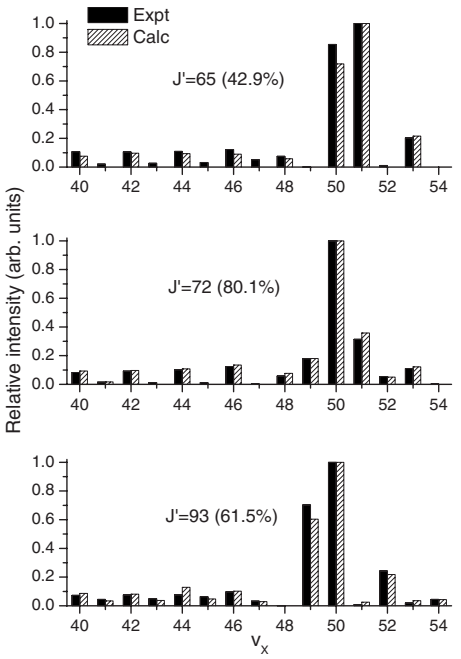

FIG. 10. The relative $A\,^1\Sigma^+ - b\,^3\Pi(v_A=26,J') \rightarrow X\,^1\Sigma^+(v_X)$ LIF progression intensity distributions observed and calculated for different rotational levels of the strongly perturbed vibronic level $v_A=26$ of the A-b complex. The number in parentheses denotes the estimated fraction (in percent) of the singlet A state. The intensities of the P and R lines are averaged and normalized to the most intensive transition of the progression.

function of the A-b complex [32]. Such a test is particularly important for confirming the vibrational numbering in the case of the NaCs molecule due to the fact that it has only one natural isotopomer $^{23}Na^{133}Cs$.

The required transition probabilities $I_{A-b\rightarrow X}$ were estimated under a Q-branch approximation ($J'=J''$) as

$$I_{A-b\rightarrow X} \sim \nu^4_{A-b\rightarrow X} M^2_{A-b\rightarrow X}, \tag{23}$$

where the fourth power in the transition wave number $\nu_{A-b\rightarrow X}=E^{CC}(J')-E_X(v_X;J'')$ is used assuming that the detector signal is proportional to the intensity of the incoming fluorescence light. The rovibronic energies $E_X(v_X;J'')$ and respective rovibrational eigenfunctions $|v_X\rangle$ of the ground $X\,^1\Sigma^+$ state were obtained by solving the single-channel radial equation with the highly accurate empirical PEC from Ref. [7].

The transition probabilities predicted for the majority of the measured $A\,^1\Sigma^+ - b\,^3\Pi(v_A \in [0,32]; J' \in [19,128]) \rightarrow X\,^1\Sigma^+(v_X;J'')$ LIF progressions agree with their experimental counterparts within the accuracy of measurements. Figure 9 presents two examples of the experimental and calculated intensity distributions in the long LIF progressions coming from the regularly perturbed vibrational levels of the $A-b$ complex, proving good agreement between measurement and calculations. It should be emphasized that the intensities of the LIF progressions originating from locally perturbed vibrational levels could also be simulated with a remarkable consistency with the experiment. Indeed, the pronounced change of the intensity distributions observed for different rotational levels $J'=65,72,93$ of the strongly perturbed vibronic level $v_A=26$ of the complex, with distinctively different triplet contribution, has been confirmed by the calculation, as shown in Fig. 10.

B. Wave numbers and probabilities of the $a \rightarrow A-b \rightarrow X$ transitions

The high accuracy achieved in the present deperturbation analysis encouraged us to simulate the transition probabilities of the $a\,^3\Sigma^+ \rightarrow A\,^1\Sigma^+ - b\,^3\Pi \rightarrow X\,^1\Sigma^+$ process, which has been proposed in Ref. [3] to transform an ultracold ensemble of Na+Cs colliding pairs into the ground level $v_X=0$; $J_X=0$ of the well bound NaCs $X\,^1\Sigma^+$ state. The appropriate population of the initial vibronically excited $a\,^3\Sigma^+(v_a;N=0)$ levels, located very close to the atomic ground-state asymptote $Na(3\,^2S)+Cs(6\,^2S)$, could be efficiently formed, for example, by the Feshbach magnetic resonance method [49].

The excitation $\nu^{pump}_{a\rightarrow A-b}$ and emission $\nu^{dump}_{A-b\rightarrow X}$ wave numbers presented in Table III correspond to the largest transition probabilities of the two-step optical conversion cycle $a\,^3\Sigma^+ \rightarrow A\,^1\Sigma^+ - b\,^3\Pi \rightarrow X\,^1\Sigma^+$. The relevant $|M^{dump}_{A-b\rightarrow X}|$ and $|M^{pump}_{A-b\leftarrow a}|$ rovibronic transition moments calculated according to the relations (21) and (22) are presented, which can be useful for estimating a required laser power of a pure Raman or STIRAP process [50]. In comparison to dump transitions, their pump counterparts have very small probabilities determined by the unfavorable transition dipole function $d_{ba}(r)$ [21,22] and small Franck-Condon factors $|\langle c_b|v_a\rangle|^2$ for weakly bound levels of the initial a-state.

TABLE III. Wave numbers $\nu^{\mathrm{pump}}_{a\to A-b}$, $\nu^{\mathrm{dump}}_{A-b\to X}$ and transition moments $|M^{\mathrm{dump}}_{A-b\to X}|$, $|M^{\mathrm{pump}}_{A-b\leftarrow a}|$ of the most favorable stimulated Raman process $a\,^3\Sigma^+(v_a;N=0)\to A\,^1\Sigma^+-b\,^3\Pi(J'=1)\to X\,^1\Sigma^+(v_X=0;J''=0)$. The $\nu^{\mathrm{pump}}_{a\to A-b}$ wave numbers are given with respect to the binding energy of the last bound level of the initial a state, namely $\Delta E_{v_a=24}\approx -0.01$ cm^{-1}. The $\tau_{A\text{-}b}$ and $R_{A\text{-}b}$ are the radiative lifetimes and branching ratios of the spontaneous emission, respectively. Numbers in brackets are the power to base 10 of the associated number.

$\nu^{\mathrm{pump}}_{a\to A-b}$ (cm^{-1})	$\nu^{\mathrm{dump}}_{A-b\to X}$ (cm^{-1})	$\lvert M^{\mathrm{pump}}_{A-b\leftarrow a}\rvert$ (a.u.)	$\lvert M^{\mathrm{dump}}_{A-b\to X}\rvert$ (a.u.)	$\tau_{A\text{-}b}$ (ns)	$R_{A\text{-}b}$ (%)
7253.73	12158.613	6.40[−3]	0.236	106	2
7161.28	12066.157	6.05[−3]	0.317	122	4
7063.20	11968.076	4.44[−3]	0.557	49	5
7350.72	12255.595	4.41[−3]	0.206	51	1
7332.06	12236.944	4.18[−3]	0.035	101	0
7425.92	12330.796	3.79[−3]	0.043	127	0
6981.14	11886.014	3.35[−3]	0.206	124	2
7455.08	12359.964	3.28[−3]	0.141	41	0
7391.71	12296.586	3.02[−3]	0.136	50	0
7492.86	12397.736	2.86[−3]	0.066	78	0
7075.95	11980.831	2.66[−3]	0.045	103	0
7521.34	12426.222	2.47[−3]	0.064	69	0
6955.13	11860.013	2.11[−3]	0.726	41	7
7560.70	12465.579	2.08[−3]	0.090	42	0
6915.45	11820.326	2.08[−3]	0.422	70	4
6817.59	11722.473	2.01[−3]	0.328	114	4
6883.65	11788.530	1.88[−3]	0.433	74	5
6734.06	11638.941	1.68[−3]	1.127	44	18
6844.88	11749.759	1.49[−3]	0.915	40	11
7622.90	12527.784	1.15[−3]	0.054	47	0
7285.68	12190.558	1.15[−3]	0.211	44	1
6629.36	11534.240	1.10[−3]	0.789	146	28
7018.55	11923.433	1.00[−3]	0.413	50	3

The $\nu^{\mathrm{pump}}_{a\to A-b}=E^{\mathrm{CC}}(J')-E_a(v_a;N=0)$ and $M^{\mathrm{pump}}_{A-b\leftarrow a}$ values were estimated using the energy $E_a(v_a;N=0)$ and wave function $|v_a\rangle$ for the last bound level of the adiabatic $a\,^3\Sigma^+$ state [7]. The $X\,^1\Sigma^+-a\,^3\Sigma^+$ mixing of the initial loosely bound levels caused by a hyperfine Fermi contact interaction [7] was neglected. The relative accuracy of the predicted transition moments can be roughly estimated as 5–10 % since it is mainly determined by the uncertainty of the *ab initio* functions $d_{AX}(r)$ and $d_{ba}(r)$ [21,22]. The accuracy of the dump wave numbers seems to be close to the accuracy of the present fit, while the accuracy of the pump wave numbers is limited by 0.1 cm^{-1} being close to the uncertainty in the dissociation energy of the $a\,^3\Sigma^+$ state [7].

Table III also contains the radiative lifetimes $\tau^{J'=1}_{A\text{-}b}$ and the branching ratios $R_{A\text{-}b}$ of the spontaneous emission from the intermediate level of the complex with $J'=1$ to the ground level $v_X=0$; $J_X=0$. Both $\tau_{A\text{-}b}$ and $R_{A\text{-}b}$ values can be useful to estimate the efficiency of a simple pump-spontaneous emission cycle for producing ground-level population. The $R_{A\text{-}b}$ values were estimated as

$$R_{A\text{-}b}=\frac{8\pi^2}{3\hbar\varepsilon_0}\nu^3_{A-b\to X}M^2_{A-b\to X}\tau^{J=1}_{A\text{-}b}, \tag{24}$$

where ε_0 is the permittivity of vacuum. The radiative lifetimes of particular rovibronic levels were estimated by the approximate sum rule [51]

$$\frac{1}{\tau^J_{A\text{-}b}}=\frac{8\pi^2}{3\hbar\varepsilon_0}\int_0^\infty dr\left[c^2_A\Delta U^3_{AX}d^2_{AX}+\sum_{\Omega=0,1,2}c^2_{b_\Omega}\Delta U^3_{ba}d^2_{ba}\right] \tag{25}$$

in order to avoid tedious summation and integration over bound and continuum vibrational levels of the lower $X\,^1\Sigma^+$ and $a\,^3\Sigma^+$ states. Here $\Delta U_{ij}(r)=U_i(r)-U_j(r)$ is the difference of the diabatic (deperturbed) PECs of the states involved.

To present better insight into how the lifetime of the rovibronic levels varies within the A-b complex, we have calculated the $\tau^J_{A\text{-}b}$ values [see Eq. (25)] dependent on the rovibronic level energy for J' values 2 and 150. The respective $\tau^J_{A\text{-}b}$ values are depicted in Fig. 11. They are strongly dependent on the degree of mixing of the mutually perturbed states since the lifetimes of the deperturbed singlet and triplet states

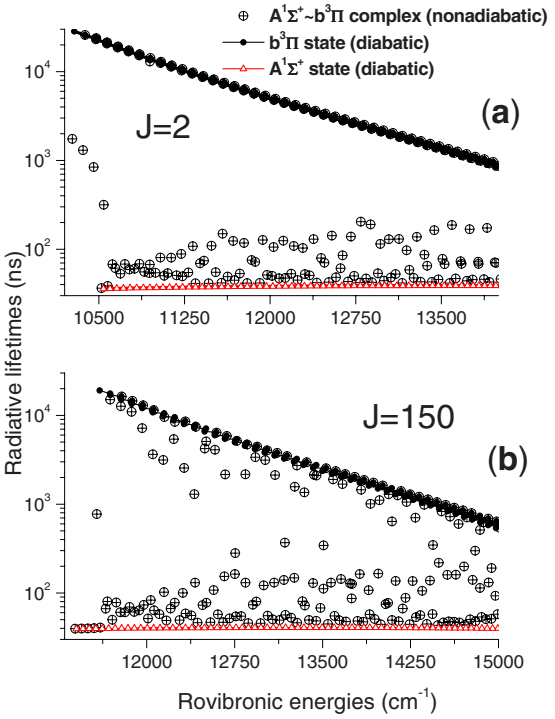

FIG. 11. (Color online) The radiative lifetimes predicted for the low ($J=2$) and high ($J=150$) rotational levels of the A-b complex as a function of the calculated nonadiabatic rovibronic energy E^{CC} of the complex.

are quite different, namely $\tau_A \approx 35$ ns $\ll \tau_b \approx 30$ μs due to $U_{AX}^3 d_{AX}^2 \gg U_{ba}^3 d_{ba}^2$. As can be seen from Fig. 11(a), for small J values the strong perturbation between the $A\ ^1\Sigma^+$ and $b\ ^3\Pi_{\Omega=0}$ component yields the mean lifetimes $\tau_{A\text{-}b}^{J=2} \approx 100$ ns for the fully mixed rovibronic levels of the complex, while weakly perturbed levels belonging to the dominant $b\ ^3\Pi_{\Omega=1,2}$ components remain the metastable ones, see the diabatic curve in Fig. 11(a). Long-living states with $\tau_{A\text{-}b}^{J=150} \approx 1-10$ μs, see Fig. 11(b), appear only for high rotational levels due to the pronounced admixture of the $b\ ^3\Pi_{\Omega=1}$ component.

V. CONCLUSIONS

Both experimental and theoretical studies of the fully mixed $A\ ^1\Sigma^+$ and $b\ ^3\Pi$ states of the NaCs molecule have been accomplished in the framework of a direct reduction of high-accuracy Fourier-transform spectroscopy data on rovibronic term values to potential-energy curves of the mutually perturbed states and spin-orbit coupling matrix elements defined analytically as expanded Morse oscillator functions of internuclear distance.

Overall 31 fitting parameters have been required to reproduce 98% of experimental term values of the A-b complex, covering rotational quantum numbers $J \in [5,151]$ within the energy range $E \in [10577, 13668]$ cm^{-1}, with a standard deviation of 0.006 cm^{-1}, which is consistent with the uncertainty of the FTS experiment. The phenomenological account for regular spin-orbit and electronic-rotational perturbations caused by the remote states manifold improved considerably the representation of rovibronic levels of the A-b complex having significant admixture of the $b\ ^3\Pi_{\Omega=1}$ component, in spite of the fact that the total number of these levels in the available data field does not exceed 2%.

The resulting molecular parameters, in principle, allow one to reproduce all term values of the A-b complex, however the accuracy of the predicted values abruptly decreases outside the experimentally studied region. The most reliable deperturbed molecular parameters apparently correspond to the singlet $A\ ^1\Sigma^+$ state and $b\ ^3\Pi_{\Omega=0}$ component of the triplet state. Simultaneous inclusion of properly weighted *ab initio* points and experimental term values into a nonlinear fitting procedure allowed us to regularize the behavior of the resulting EMO PECs and SO functions at small and large internuclear distances.

The derived empirical PECs are found to be rather close, within 1–2 vibrational quanta, to their *ab initio* counterparts [20–22] near the equilibrium distances. The derived SO matrix elements coincide with the recent *ab initio* estimates [22] within 10–15 cm^{-1} inside the present limited experimental data region.

The term values-based deperturbation analysis performed on a sole natural ^{23}Na^{133}Cs isotopomer was confirmed by a simulation of relative intensity distributions in $A-b(v_A;J') \rightarrow X(v_X;J'')$ LIF progressions originating from both weakly and strongly perturbed, low and high vibrational levels of the complex.

Calculations of the transition probabilities show that, in contrast to the emission (dump) step, the absorption (pump) step of the suggested [3] two-step optical conversion cycle $a\ ^3\Sigma^+(v_a;N=0) \rightarrow A\ ^1\Sigma^+ - b\ ^3\Pi(J'=1) \rightarrow X\ ^1\Sigma^+(v_X=0;J''=0)$ requires a high-power laser source generating in the currently unfavorable IR spectral range.

ACKNOWLEDGMENTS

The authors are indebted to A. Pashov for providing the program package for identification and analysis of LIF progressions. The authors are grateful to O. Martinsons for participation in the experiments and to O. Docenko for her help in preparation of the manuscript. Financial support by the Latvian University basic research funds, as well as from the Latvian Science Council (Grant No. 04.1308), is gratefully acknowledged by the Riga team. The Moscow team is grateful for support from the Russian Foundation for Basic Research (Grant No. 06-03-32330a).

[1] F. Masnou-Seeuws and P. Pillet, Adv. At., Mol., Opt. Phys. **47**, 53 (2001).
[2] J. Doyle, B. Friedrich, R. V. Krems, and F. Masnou-Seeuws, Eur. Phys. J. D **31**, 149 (2004).
[3] W. C. Stwalley, Eur. Phys. J. D **31**, 221 (2004).
[4] T. Bergeman, A. J. Kerman, J. Sage, S. Sainis, and D. DeMille, Eur. Phys. J. D **31**, 179 (2004).
[5] O. Docenko, M. Tamanis, R. Ferber, A. Pashov, H. Knöckel, and E. Tiemann, Eur. Phys. J. D **31**, 205 (2004).
[6] O. Dulieu, M. Raoult, and E. Tiemann, J. Phys. B **39**, 1 (2006).
[7] O. Docenko, M. Tamanis, J. Zaharova, R. Ferber, A. Pashov, H. Knöckel, and E. Tiemann, J. Phys. B **39**, S929 (2006).
[8] D. DeMille, Phys. Rev. Lett. **88**, 067901 (2002).
[9] T. Bergeman, C. E. Fellows, R. F. Gutterres, and C. Amiot, Phys. Rev. A **67**, 050501(R) (2003).
[10] A. J. Kerman, J. M. Sage, S. Sainis, T. Bergeman, and D. DeMille, Phys. Rev. Lett. **92**, 153001 (2004).
[11] J. M. Sage, S. Sainis, T. Bergeman, and D. DeMille, Phys. Rev. Lett. **94**, 203001 (2005).
[12] E. R. Hudson, N. B. Gilfoy, S. Kotochigova, J. M. Sage, and D. DeMille, Phys. Rev. Lett. **100**, 203201 (2008).
[13] C. Haimberger, J. Kleinert, M. Bhattacharya, and N. P. Bigelow, Phys. Rev. A **70**, 021402(R) (2004).
[14] C. Haimberger, J. Kleinert, O. Dulieu, and N. P. Bigelow, J. Phys. B **39**, S957 (2006).
[15] J. Deiglmayr, A. Grochola, M. Repp, K. Mörtlbauer, C. Glück, J. Lange, O. Dulieu, R. Wester, and M. Weidemüller, Phys. Rev. Lett. **101**, 133004 (2008).
[16] K. B. S. Eriksson and I. Wenaker, Phys. Scr. **1**, 21 (1970).
[17] K.-H. Weber and C. J. Sansonetti, Phys. Rev. A **35**, 4650 (1987).
[18] J. P. Shaffer, W. Chalupczak, and N. P. Bigelow, Phys. Rev. Lett. **82**, 1124 (1999).
[19] J. Zaharova, O. Docenko, M. Tamanis, R. Ferber, A. Pashov, H. Knöckel, and E. Tiemann, J. Chem. Phys. **127**, 224302 (2007).
[20] M. Korek, A. R. Allouche, K. Fakhreddine, and A. Chaalan, Can. J. Phys. **78**, 977 (2000).
[21] M. Aymar and O. Dulieu, Mol. Phys. **105**, 1733 (2007).
[22] A. V. Stolyarov and J. T. Kim (unpublished).
[23] I. Klincare, J. Zaharova, M. Tamanis, R. Ferber, A. Zaitsevskii, E. A. Pazyuk, and A. V. Stolyarov, Phys. Rev. A **76**, 032511 (2007).
[24] S. Magnier and Ph. Millié, Phys. Rev. A **54**, 204 (1996).
[25] M. Korek, S. Bleik, and A. R. Allouche, J. Chem. Phys. **126**, 124313 (2007).
[26] H. Lefebvre-Brion and R. W. Field, *The Spectra and Dynamics of Diatomic Molecules* (Academic, New York, 2004).
[27] P. Qi, J. Bai, E. Ahmed, A. M. Lyyra, S. Kotochigova, A. J. Ross, C. Effantin, P. Zalicki, J. Vigué, G. Chawla, R. W. Field, T.-J. Whang, W. C. Stwalley, H. Knöckel, E. Tiemann, J. Shang, L. Li, and T. Bergeman, J. Chem. Phys. **127**, 044301 (2007).
[28] M. R. Manaa, A. J. Ross, F. Martin, P. Crozet, A. M. Lyyra, Li Li, C. Amiot, and T. Bergeman, J. Chem. Phys. **117**, 11208 (2002).
[29] C. Amiot, O. Dulieu, and J. Verges, Phys. Rev. Lett. **83**, 2316 (1999).
[30] H. Salami, T. Bergeman, A. J. Ross, P. Crozet, B. Beser, J. Bai, A. M. Lyyra, S. Kotochigova, D. Li, F. Xie, L. Li, and O. Dulieu, in *Book of Abstracts of the XXI International Conference on Atomic Physics* (ICAP2008, Storrs, CT, 2008), p. 68.
[31] M. Tamanis, R. Ferber, A. Zaitsevskii, E. A. Pazyuk, A. V. Stolyarov, H. Chen, J. Qi, H. Wang, and W. C. Stwalley, J. Chem. Phys. **117**, 7980 (2002).
[32] A. Jarmola, M. Tamanis, R. Ferber, E. A. Pazyuk, and A. V. Stolyarov, J. Quant. Spectrosc. Radiat. Transf. **95**, 165 (2005).
[33] O. Docenko, M. Tamanis, R. Ferber, E. A. Pazyuk, A. Zaitsevskii, A. V. Stolyarov, A. Pashov, H. Knöckel, and E. Tiemann, Phys. Rev. A **75**, 042503 (2007).
[34] L. D. Landau and E. M. Lifshitz, *Quantum Mechanics* (Pergamon, New York, 1965).
[35] O. Docenko, M. Tamanis, R. Ferber, A. Pashov, H. Knöckel, and E. Tiemann, Phys. Rev. A **69**, 042503 (2004).
[36] A. Pashov, O. Docenko, M. Tamanis, R. Ferber, H. Knöckel, and E. Tiemann, Phys. Rev. A **72**, 062505 (2005).
[37] See EPAPS Document No. E-PLRAAN-78-112812 for a full list of experimental term values. For more information on EPAPS, see http://www.aip.org/pubservs/epaps.html.
[38] V. V. Meshkov, A. Zaitsevskii, E. A. Pazyuk, A. V. Stolyarov, R. Bruhl, and D. Zimmermann, J. Chem. Phys. **123**, 204307 (2005).
[39] H. Katô, Bull. Chem. Soc. Jpn. **66**, 3203 (1993).
[40] J. Zaharova, O. Nikolayeva, M. Tamanis, M. Auzinsh, R. Ferber, A. Zaitsevskii, E. A. Pazyuk, and A. V. Stolyarov, J. Chem. Phys. **124**, 184318 (2006).
[41] E. G. Lee, J. Y. Seto, T. Hirao, P. F. Bernath, and R. J. LeRoy, J. Mol. Spectrosc. **194**, 197 (1999).
[42] R. J. Le Roy, A computer program to fit pointwise potentials to selected analytic functions. http://leroy.uwaterloo.ca/programs University of Waterloo Chemical Physics Research Report CP-663R (2007).
[43] I. Dabrowski, D. W. Tokaryk, and J. K. G. Watson, J. Mol. Spectrosc. **189**, 95 (1998).
[44] W. H. Press, S. A. Teukolsky, W. T. Vetterling, and B. P. Flannery, *Numerical Recipes in Fortran 77* (Cambridge University Press, Cambridge, UK, 1999).
[45] J. More, B. Garbow, and K. Hillstrom, MINPACK software for solving nonlinear equations and nonlinear least-squares problems. http://www.netlib.org/minpack, University of Chicago, Argonne National Laboratory (1999).
[46] V. V. Meshkov, A. V. Stolyarov, and R. J. LeRoy, Phys. Rev. A **78**, 052510 (2008).
[47] D. G. Truhlar, J. Comput. Phys. **10**, 123 (1972).
[48] R. B. Lenoucq, D. C. Sorensen, and C. Yang, ARPACK User's Guide: Solution of Large Scale Eigenvalue Problems with Implicitly Restarted Arnoldi Methods (1997); http://www.netlib.org/arpack.
[49] V. Vuletić, A. J. Kerman, C. Chin, and S. Chu, Phys. Rev. Lett. **82**, 1406 (1999).
[50] K. Bergmann, H. Theuer, and B. W. Shore, Rev. Mod. Phys. **70**, 1003 (1998).
[51] T. Kiyoshima, S. Sato, E. A. Pazyuk, A. V. Stolyarov, and M. S. Child, J. Chem. Phys. **118**, 121 (2003).